

Effects of Radial Distances on Small-scale Magnetic Flux Ropes in the Solar Wind

YU CHEN¹ AND QIANG HU²

¹*Department of Space Science
The University of Alabama in Huntsville
Huntsville, AL 35805, USA*

²*Department of Space Science
Center for Space Plasma and Aeronomic Research (CSPAR)
The University of Alabama in Huntsville
Huntsville, AL 35805, USA*

(Received 01/23/2020; Revised 03/16/2020; Accepted)

Submitted to AJ

ABSTRACT

Small-scale magnetic flux ropes (SFRs), in the solar wind, have been studied for decades. Statistical analysis utilizing various in situ spacecraft measurements is the main observational approach which helps investigate the generation and evolution of these small-scale structures. Based on the Grad-Shafranov (GS) reconstruction technique, we use the automated detection algorithm to build the databases of these small-scale structures via various spacecraft measurements at different heliocentric distances. We present the SFR properties including the magnetic field and plasma parameters at different radial distances from the sun near the ecliptic plane. It is found that the event occurrence rate is still in the order of a few hundreds per month, the duration and scale size distributions follow power laws, and the flux rope axis orientations are approximately centered around the local Parker spiral directions. In general, most SFR properties exhibit radial decays. In addition, with various databases established, we derive scaling laws for the changes of average field magnitude, event counts, and SFR scale sizes, with respect to the radial distances, ranging from ~ 0.3 au for Helios to ~ 7 au for the Voyager spacecraft. The implications of our results for comparisons with the relevant theoretical works and for the application to the Parker Solar Probe (PSP) mission are discussed.

Corresponding author: Qiang Hu
qiang.hu@uah.edu, qiang.hu.th@dartmouth.edu

Keywords: solar wind — turbulence — magnetohydrodynamics (MHD) — methods: data analysis

1. INTRODUCTION

In the past few decades, there has been a number of observational studies on small-scale magnetic flux ropes (hereafter, SFRs) in the solar wind. These relatively small-scale structures, first identified from the *Ulysses* spacecraft measurements at ~ 5 au by [Moldwin et al. \(1995\)](#), generally are believed to have the same helical magnetic field configuration as their large-scale counterparts, i.e., magnetic clouds (MCs). Employing various in-situ spacecraft mission datasets, such as those from *IMP-8*, *WIND* and *STEREO* at about 1 au, a limited number (usually in the order of hundreds in total at most) of SFRs were identified for multiple years via mostly visual inspection or semi-automated method. For example, [Cartwright & Moldwin \(2010\)](#) used *Helios 1 & 2*, *IMP-8*, *WIND*, *ACE* and *Ulysses* spacecraft datasets with the corresponding heliocentric distances ranging from ~ 0.3 to 5.5 au to investigate the occurrence and the evolution of hundreds of SFRs. This represents the first comprehensive study of SFRs and the generation of SFR databases from multiple spacecraft missions, although the event counts are very limited. The corresponding statistical studies on these limited-size samples suggested that these small structures can last for about tens of minutes up to a few hours, and thus have smaller scale sizes over their cross sections as compared with magnetic clouds ([Moldwin et al. 2000](#)).

In the meanwhile, the distinctions between the two populations were sought out, and the two possible sources, i.e., small coronal mass ejection (CME) from solar eruption and magnetic reconnection across the heliospheric current sheet (HCS) in the solar wind, were proposed to be origins of SFRs ([Feng et al. 2007, 2008](#); [Cartwright & Moldwin 2008](#)). In addition, [Yu et al. \(2016\)](#); [Yu et al. \(2014\)](#) performed careful and detailed analysis of in-situ observations of small transients (STs) including SFRs in the solar wind around 1 au. They examined their overall magnetic and plasma properties, and concluded that these relatively small-scale structures may originate from both the solar corona and the interplanetary medium.

One step forward in the study of SFRs is the implementation of automated and computerized algorithm, based on the Grad-Shafranov (GS) reconstruction technique, for identifying these structures from in-situ spacecraft measurements. This has yielded significantly more number of events, which is more substantial for statistical investigations. The GS method (see [Hu 2017](#), for a comprehensive review) is a unique data analysis technique capable of recovering the two dimensional (2D) structure from one dimensional (1D) time series data ([Sonnerup & Guo 1996](#); [Hau & Sonnerup 1999](#); [Hu & Sonnerup 2001](#); [Hu & Sonnerup 2002](#)). [Zheng & Hu \(2018\)](#) created the computer-based program to identify SFRs automatically. This automated detection has succeeded in finding 74,241 SFRs by using the *WIND* spacecraft in situ mea-

measurements from 1996 to 2016 (Hu et al. 2018). By this abundant event count number (in the order of a few hundreds per month on average), they compared the monthly counts of SFRs with the corresponding sunspot numbers and indicated that the occurrence of SFRs has obvious solar cycle dependency with a short lag. Later, this automated detection was applied to the *ACE* and *Ulysses* measurements (Chen et al. 2019). The bulk properties of identified SFRs, including the magnetic field strength and plasma parameters, are presented in terms of their variations with time, heliographic latitudes and radial distances. It is found that the solar cycle dependency or the temporal variation of SFRs appears to be affected by both latitudinal and radial-distance changes owing to the unique orbit of *Ulysses*. An earlier study on par with the number of events identified by the GS-based approach was performed by Borovsky (2008) using *ACE* measurements to identify boundaries of about 65,860 flux tubes for seven years worth of data. That study suggested that these flux tubes are tangled along the Parker spiral direction and forming a scenario made up of “spaghetti” like structures originating from the Sun.

On the other hand, the other relevant studies have hinted at the local generation of these flux tube/rope structures from 2D magnetohydrodynamic (MHD) turbulence. These 2D turbulence is characterized by quasi-2D coherent structures manifested as current sheets and flux ropes of variable sizes, corresponding to spatial scales in the inertia range (Matthaeus et al. 2007; Servidio et al. 2008; Wan et al. 2013; Zank et al. 2017). Various studies using in-situ spacecraft measurements (e.g., Greco et al. 2008, 2009; Osman et al. 2014; Greco et al. 2018) were carried out for identifying and characterizing discontinuities, i.e., current sheets, which may be considered as proxies to boundaries (or so-called “walls”) of flux ropes. In particular, the partial variance of increments (PVI) method is commonly used to identify discontinuities from in situ magnetic field measurements (see the review by Greco et al. (2018)). For instance, the correspondence between the distributions of the wall-to-wall time of SFRs and the waiting time of current sheets yielded consistent results in determining the correlation length scale for 2D MHD turbulence (Zheng & Hu 2018; Greco et al. 2009). Recently, Pecora et al. (2019) examined *WIND* in situ data and related the SFRs and current sheets by combing the GS reconstruction and the PVI methods. They showed the correspondence between the flux rope boundaries and current sheets, where each type of structures was identified from the same dataset but with different and independent approaches. They certified again that these small-scale structures can be generated self-consistently from quasi-2D MHD turbulence.

To further extend and complete our SFR event databases for the existing and past spacecraft missions, we apply our automated detection algorithm to *Helios 1 & 2* and *Voyager 1 & 2* datasets in the present study. Considering that they offer observations at additional heliocentric distances complementary to the *ACE* and *Ulysses* missions, we will also perform a comprehensive analysis of the possible evolution of

SFR properties with radial distances between ~ 0.3 and 8 au, especially for a uniquely controlled subset of events to be described below.

This paper is organized as follows. The method of the automated detection will be described briefly together with the data selection for this study in Section 2. In Section 3, the SFRs identified from the full *Helios* mission is categorized into three groups by their corresponding heliocentric distances. One specific year is selected for identification via the *Voyager* mission. The SFRs properties including the axis orientation angles, the magnetic field and plasma parameters, the duration and scale size will be discussed for each event set, respectively. In Section 4, the radial distributions of SFRs via these two missions as well as *ACE* and *Ulysses* are presented. The radial effects associated with the possible scenario of flux rope merging are discussed. The findings and additional discussions, in particular, regarding the applications to the *Parker Solar Probe (PSP)* mission, are summarized in the last section.

2. METHOD AND DATA SELECTION

The data analysis method we employ is the recently developed automated flux-rope detection algorithm based on the Grad-Shafranov (GS) reconstruction technique. The GS reconstruction method is an advanced data analysis tool based on the two-dimensional (2D) GS equation describing space plasma structures in approximate 2D quasi-static equilibrium and employing in-situ spacecraft measurements. It has been widely applied to various space plasma regimes by a number of research groups worldwide for over twenty years (see Hu 2017, for a comprehensive review). The latest development has been the application of the basic GS reconstruction procedures to identifying relatively small-scale magnetic flux ropes (SFRs) in the solar wind in a completely computerized and automated manner (Zheng & Hu 2018; Hu et al. 2018; Chen et al. 2019). This has enabled the generation of exhaustive event lists for the flagship NASA solar-terrestrial spacecraft missions. The event occurrence rate is in the order of a few hundreds per month, which had not been achieved by other means before. The detailed documentation of the approach including an algorithm flowchart was provided in Hu et al. (2018), which should enable the implementation of the algorithm by interested users on their own. We provide below a brief description of the basic concepts underlying the automated detection algorithm, which is also utilized in the current study.

The basic quantity characterizing the 2D flux rope configuration is defined through a magnetic flux function, $A(x, y)$, which fully characterizes the transverse magnetic field on the cross-section plane (x, y) , perpendicular to the flux rope axis, z . In other words, the isosurfaces of A , i.e., where $A = \text{const}$, represent flux surfaces on which the magnetic field lines are winding along the central axis z with $B_z \neq 0$ and $\partial/\partial z \approx 0$. Therefore a solution of the scalar function A , governed by the GS equation, as well as a non-vanishing axial field component $B_z(A)$ fully characterizes a cylindrical flux rope configuration with nested flux surfaces surrounding one central

z axis. Thus one important property associated with such a configuration is the single-valued behavior of the so-called field-line invariants, i.e., a few quantities as single-variable functions of A only, i.e., also being constant on each flux surface. They include the axial field component B_z , the plasma pressure p , and the transverse pressure $P_t = p + B_z^2/2\mu_0$. These quantities together with the A values all can be directly evaluated along a single spacecraft path once a z axis is chosen. For a cylindrical flux rope configuration and a spacecraft path across multiple nested flux surfaces, these quantities, as single-variable functions of A , all exhibit a discernable double-folding behavior when displayed against A values along the path. This is because along the spacecraft path, each flux surface is crossed twice by the spacecraft, once along the inbound (“1st” half of the) path, while the other outbound (or the “2nd” half). Therefore the corresponding pairs of A values are the same because each is on the same flux surface. So is each pair of the corresponding invariant quantity, as single-variable function of A , thus leading to the behavior such that the “2nd” half of the data points folds and overlaps with the “1st” half, becoming so-called double-folding.

The A values along the spacecraft path (at $y = 0$) generally exhibit a monotonically increasing or decreasing pattern along the “1st” half, then the trend reverses for the “2nd” half, after an extremum is reached. These values $A(x, 0)$ are calculated from the “rotating” component of the magnetic field via $A(x, 0) = -\int_0^x B_y d\xi$, where the spatial increment $d\xi = -\mathbf{V}_F \cdot \hat{\mathbf{x}} dt$ is related to a frame velocity \mathbf{V}_F (commonly the average solar wind velocity) and the time increment dt of the time-series data. The point at which the value $A(x, 0)$ reaches an extremum is called the turning point. It is also where the component B_y changes sign, separating the “1st” and the “2nd” halves. Therefore the resulting double-folding behavior in the field-line invariants, as dictated by the GS equation, constitutes the key feature we utilize to devise the algorithm for detecting magnetic flux rope intervals from in-situ spacecraft measurements. The quality of the “double-folding” pattern is assessed quantitatively by several metrics to result in the identification of flux rope candidates. These metrics include the definition of two residues evaluating primarily the goodness of the satisfaction for these quantities, in particular the transverse pressure P_t , being single-valued and double-folded. A Walén slope threshold is also used to exclude mostly Alfvénic fluctuations. In addition, an optional threshold condition on the average magnetic field magnitude over a candidate event interval can also be applied to reduce contamination of small-amplitude fluctuations whose flux-rope characteristics are less certain. The detailed descriptions of the procedures were provided in [Hu et al. \(2018\)](#). We refer interested readers to that report for further details.

The automated detection algorithm has been applied to a number of in-situ spacecraft missions, including ACE, Wind, and Ulysses ([Hu et al. 2018](#); [Chen et al. 2019](#)). A designated website containing the event databases is available at <http://fluxrope.info>. Due to the implementation of the highly computerized algo-

Table 1. Spacecraft Missions for the Small-scale Magnetic Flux Rope Detection and Analysis.

Spacecraft	Helios 1	Helios 2	ACE	Ulysses	Voyager 1 (2)
Periods (years)	1975-1984	1976-1980	1998-2018	1991-2009	1980
Counts	15,041	7,981	38,505	22,719	1,480 (1,991)

rithm and the usage of cluster machines, the analysis of whole mission dataset becomes feasible. We continue our analysis in this study for additional in-situ spacecraft datasets in the heliosphere, specifically the Helios and Voyager missions. The specific time periods and the resulting event counts for each mission are listed in Table 1. Since we focus on studying the flux rope properties at different heliocentric distances and attempt to inter-relate these properties considered to be radially distributed in the solar wind, we select as many as possible the periods when data are available for the whole Helios mission, but only include year 1980 for the Voyagers when they were at large radial distances, but still in low helio-latitudes near the ecliptic. Such selections are also largely affected by the data integrity issues, i.e., the existence of data gaps. When they are prevalent, especially for plasma parameters which are required in our analysis, and for relatively historical missions, the data integrity is significantly reduced and negatively impacts the search results greatly. Nonetheless, on average, the event occurrence rate is still in the order of a few thousands a year, owing to the fairly exhaustive detection approach, by using 1-minute cadence data throughout (Hu et al. 2018).

3. ANALYSIS RESULTS

The analysis on a number of heliospheric missions as listed in Table 1 was carried out systematically for all available data, except for the Voyager mission. Due to data integrity issues both concerning the low-quality or missing data and insufficient resolution of the time series, the analysis results for Voyagers are limited to year 1980 only. At that time, the spacecraft were at a heliocentric distance ~ 6.05 - 9.57 au near the ecliptic plane. The event counts from the Helios mission are also relatively lower mostly due to significant number of data gaps. In Section 3.1, we present the properties of identified SFRs for Helios and Voyager missions, respectively. The detailed descriptions of Ulysses, ACE and Wind results were already reported elsewhere in Chen et al. (2019) and Hu et al. (2018). In Section 3.2, we present the results from a subset of events for all four missions under similar condition of over exact one-year time period near the ecliptic plane, but at different heliocentric distances.

3.1. Distributions of Selected Flux Rope Properties at Different Radial Distances

We have reported the comprehensive analysis of SFR databases generated for the Wind/ACE and Ulysses spacecraft missions before. Here we have applied the automated detection algorithm to the Helios and Voyager missions for the first time. The Helios mission, consisting of two identical probes, took an elliptical orbit deep into

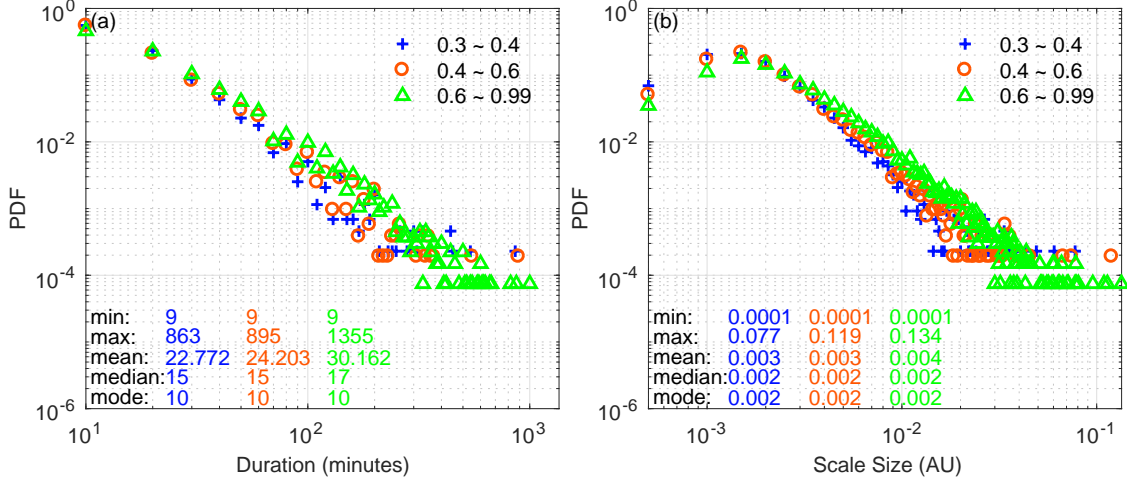


Figure 1. The (a) duration and (b) scale size distributions of SFRs for Helios 1 & 2. The events from both spacecraft are divided into three groups according to the radial distances in au, as indicated by the legend. The statistical quantities for each distribution are also denoted in each panel.

the inner heliosphere around the Sun with a perihelion around 0.3 au. Thus it had provided the in-situ measurements of solar wind parameters in the range of heliocentric distances between ~ 0.3 and 0.99 au over the whole mission spanning years 1975 to 1984. We found a total number of 15,041 SFR intervals for Helios 1 and 7,981 for Helios 2, respectively, with the search window size (or duration) ranging from 9 to 2255 minutes. Figure 1 shows the distributions in terms of the probability density functions (PDFs) of the duration and the corresponding cross-section scale sizes of identified SFRs, taking into account the orientation of each identified cylindrical flux rope, relative to the spacecraft path. They are divided into three groups according to the ranges of radial distances in au as indicated by the legend. The maximum duration rarely exceeds 1000 minutes, due to the relatively frequent occurrence of data gaps. The distributions of duration for smaller values, i.e., < 100 minutes, appear to exhibit power laws. Such trends seem to only persist for scale sizes within a narrow range $\sim [0.002, 0.01]$ au.

Figure 2 shows the distributions of orientation angles of the flux rope cylindrical axis z for the three groups, separately. Figure 2a shows the histograms of the polar angle distributions overplotted for the three groups, as indicated by the legend, corresponding to events identified at different radial distances. They all tend to have increasing counts toward $\theta \approx 90^\circ$, i.e., increasingly more events with smaller inclination angles with respect to the ecliptic plane. Figure 2b shows the corresponding distributions of the azimuthal angles, ϕ , measured with respect to the positive R axis for the z axis projected onto the TN plane. The distributions are folded into the range $[0^\circ, 180^\circ]$ such that this angle measures the smaller angle between the projected z axis onto the TN plane and the positive R axis. Unlike the clear tendency in the polar angle distributions, the azimuthal angle ϕ has a less clear tendency and is more broadly

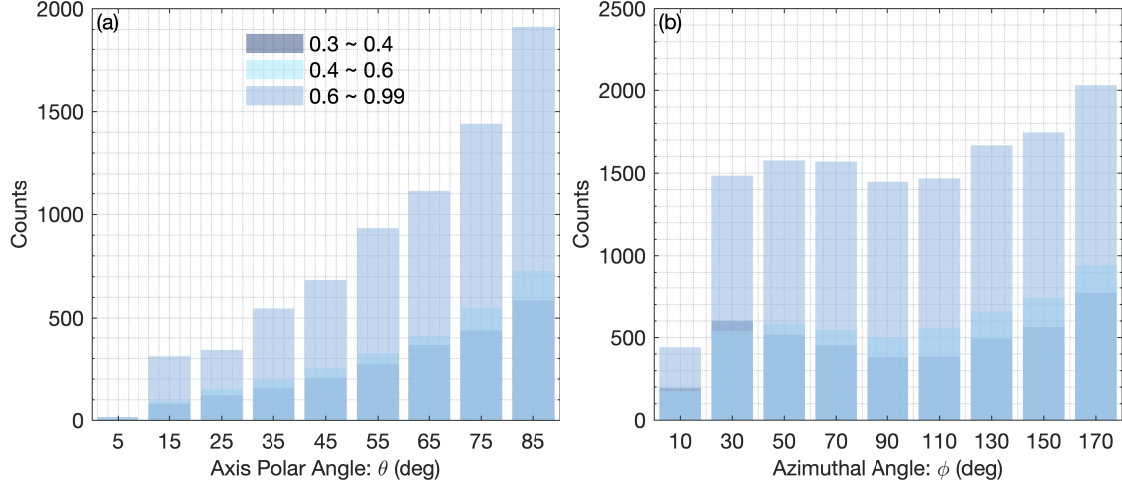


Figure 2. The distributions of the directional angles of the flux rope axis from the Helios event set: (a) the polar angle θ in degrees, and (b) the azimuthal angle ϕ in degrees, as measured in the spacecraft centered *RTN* coordinates. Different shades represent the subgroups of events separated by the corresponding radial distances in au as indicated by the legend in panel (a).

distributed, although it still tends to peak near one end about 170° and the other around $30\text{-}50^\circ$. This behavior is likely owing to the wide range of radial distances where these event were identified. A strict Parker spiral angle distribution would correspond to azimuthal angles changing from near 0° or 180° near the Sun to about 45° or 135° near 1 au. Such a trend is somewhat embedded in Figure 2b.

Figure 3 shows the distributions of various flux rope properties averaged over each flux rope interval for all Helios events, again separated into the three groups as before. The radial decay in the average field magnitude $\langle B \rangle$, and in proton number density are readily seen. On the other hand, the changes in proton temperature and the resulting proton β are less pronounced. Especially for the two groups with radial distances in the range < 0.6 au, the distributions are nearly identical. For all three groups, the mean proton β values are all around 0.5.

For Voyagers, due to the data integrity issue and the constraint that we mainly focus on low-latitude observations in this report, only the data in year 1980 for both Voyager 1 and 2 are analyzed. The total number of events is very limited compared with other missions. Therefore the statistical significance in the distributions of relevant flux rope properties is also much reduced. Nonetheless for completeness, we present the same set of parameters representative of flux rope properties for the first time at the heliocentric distance around and beyond 6 au near the ecliptic. Figure 4 shows the distributions of duration and scale size. The power-law trend is not clear due to the relatively large scattering of the data points and low counts. Figure 5 shows the corresponding distributions of selected parameters averaged over flux rope intervals, similar to Figure 3. The decreases in the magnitudes of $\langle B \rangle$, $\langle T_p \rangle$, and $\langle N_p \rangle$ are evident at such a large radial distance away from the Sun. However the resulting proton $\langle \beta \rangle$ remains modest, with an order of magnitude ~ 0.1 on average, even at this

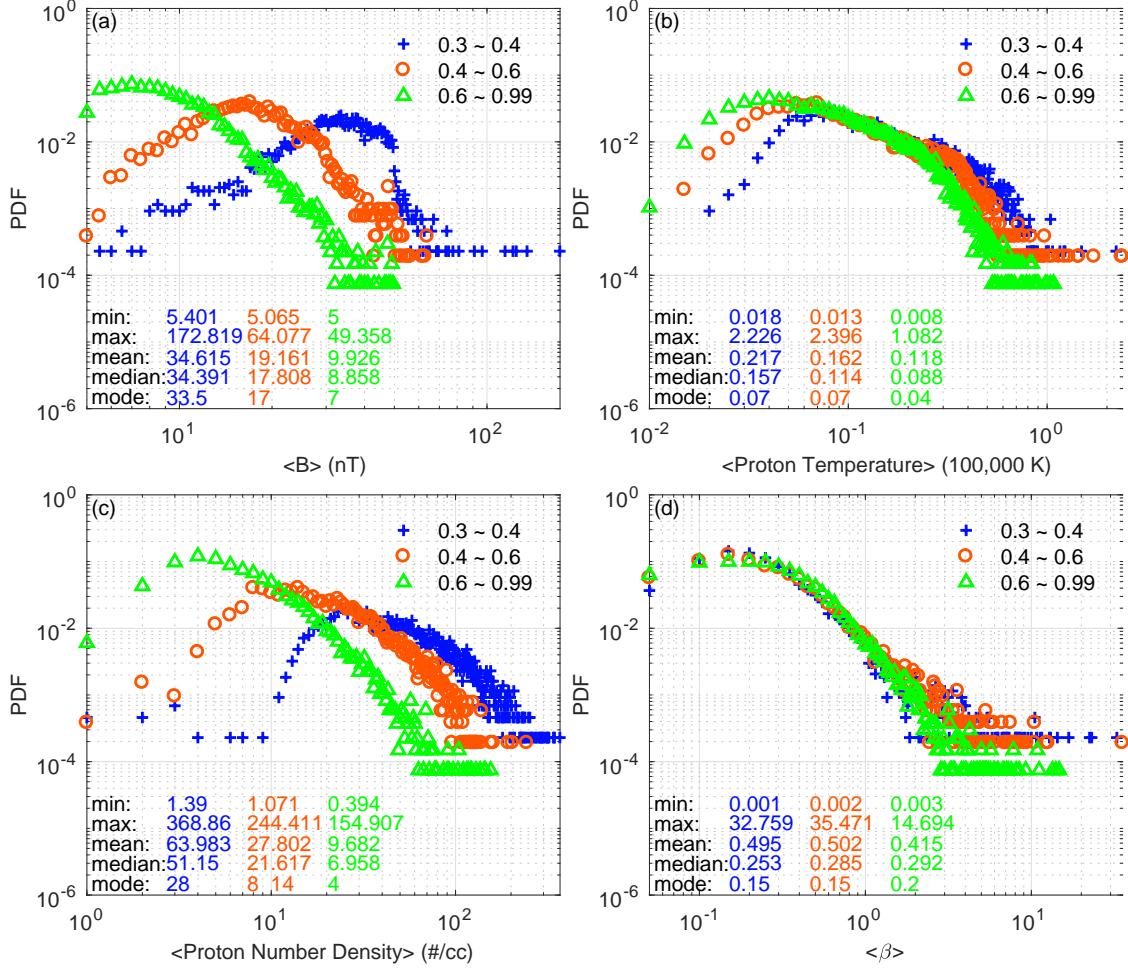


Figure 3. The distributions of flux rope properties derived from each flux rope interval identified from both Helios 1 & 2: (a) the average field magnitude, (b) the average proton temperature, (c) the average proton number density, and (d) the average proton β . Different symbols represent the corresponding subgroups of SFR events identified with the radial distance range as indicated by the legend. The statistical quantities for each distribution are also denoted in each panel.

radial distance. The flux rope axis orientation angle distributions, given in Figure 6, indicate a trend with more events lying on the ecliptic plane along the nominal Parker spiral direction. The counts for the z axis polar angle gradually increase toward 90° , while the corresponding azimuthal angle distribution has a broad peak around 90° (the direction perpendicular to the radial direction).

It is worth noting that we were not able to present the statistical results of waiting time and wall-to-wall time distributions (see, e.g., Zheng & Hu 2018) for both Helios and Voyager missions because of wide-spread data gaps. These gaps will interfere with the distributions of these two quantities.

3.2. Radial Distributions of Flux Rope Properties Under Similar Conditions

To further investigate the variation of SFR properties at different radial distances, here we select a subset of events from each spacecraft mission. Each spans a time

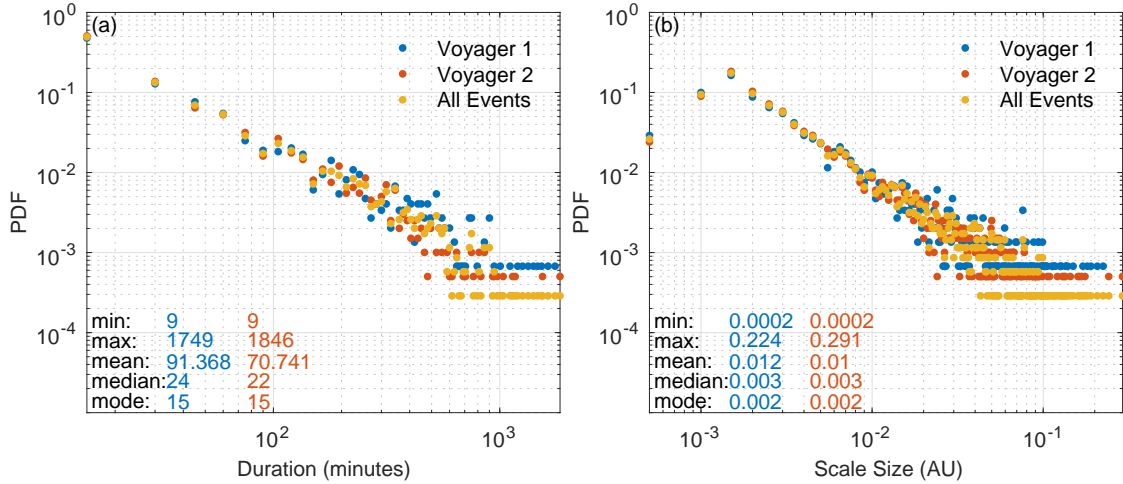


Figure 4. The distributions of SFR duration and scale size for Voyager event set. Format is the same as Figure 1. See legend for different groups.

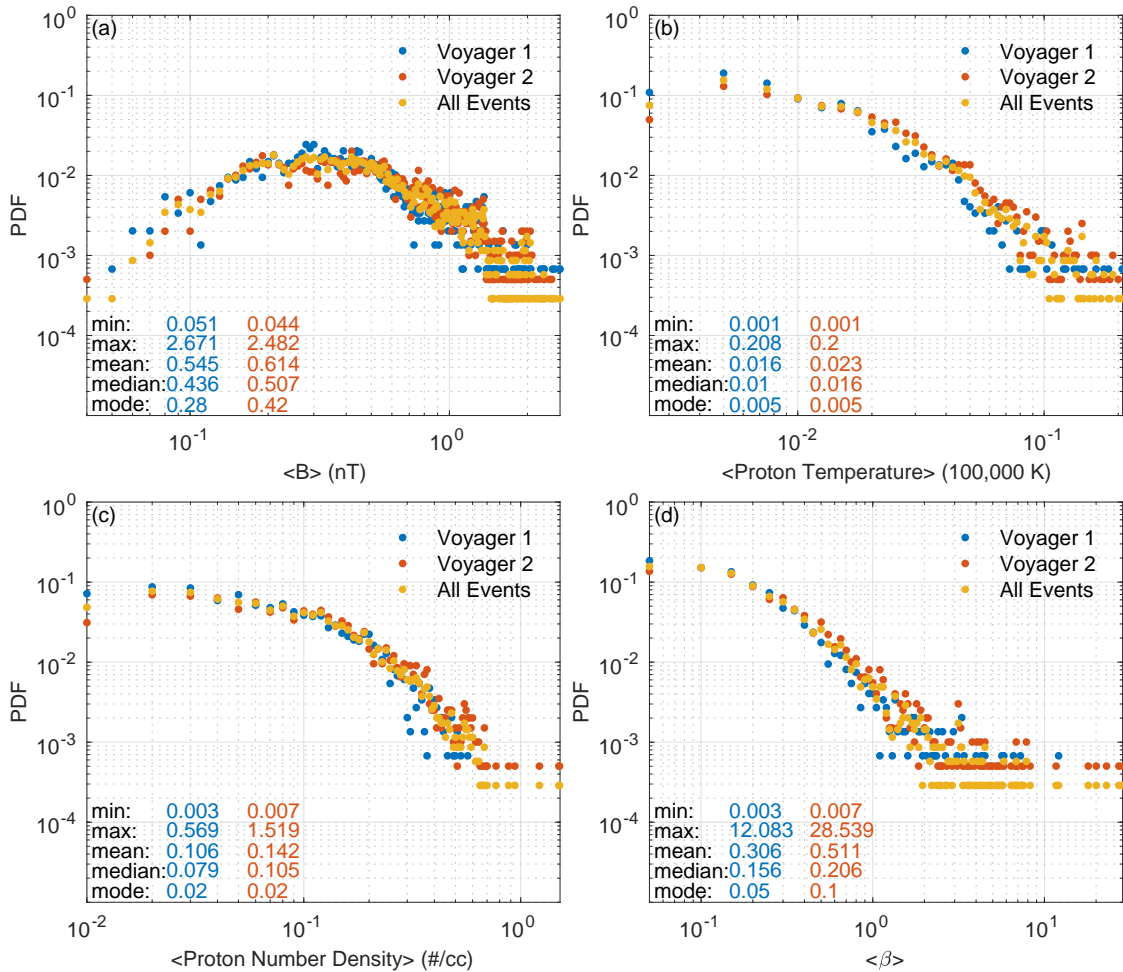


Figure 5. The distributions of SFR properties for Voyagers. Format is the same as Figure 3.

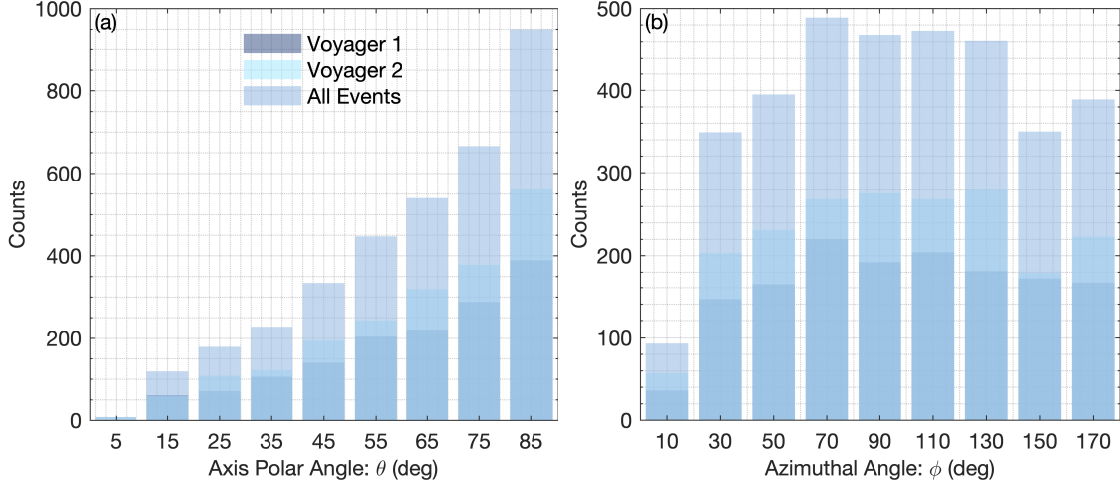


Figure 6. The distributions of directional angles of flux rope axis for Voyagers. Format is the same as Figure 2 (but see the legend in a).

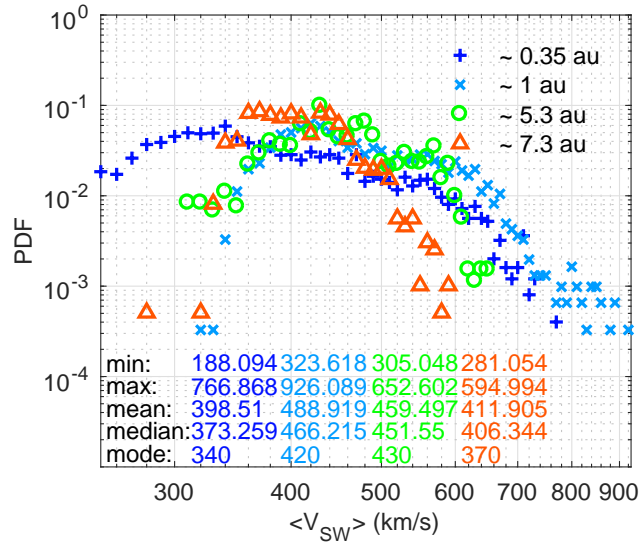


Figure 7. The distributions of the average solar wind speed, $\langle v_{sw} \rangle$, for events listed in Table 2. See legend for the correspondence of symbols to different spacecraft missions at varying heliocentric distances near the ecliptic.

period of the same length, i.e., one year, to facilitate intercomparison among the selected flux rope properties under similar conditions, except for being radially distributed. For example, Figure 7 shows the average solar wind velocity distributions in those flux rope intervals. The distributions are similar if we exclude the counts in single-digit numbers. They mostly lie in the range between 300 and 600 km/s, with the notable exception for Helios whose counts extend well into the low-speed wind regime.

The selection criteria and the resulting event counts are listed in Table 2. In a previous study by Hu et al. (2018), the possible effect of radial distances on SFRs via ACE and Ulysses measurements was reported. Now, with more available databases we

plan to further extend that study by selecting specific years for four in situ datasets. Specifically, in Table 2, we present the basic information and special criteria applied to these four sets of measurements: (1) For Helios, we select SFR records detected in less than 0.4 au for both spacecraft and set a lower limit of magnetic field magnitude to be 25 nT to remove small fluctuations. (2) For ACE & Ulysses, the year 2004 is selected since it is one of the years when Ulysses was at low latitudes (less than 30°) and at far radial distances. (3) For Voyagers, Year 1980 is selected. Specifically, we select a three-month period when Voyager 1 traveled from 6.9 to 7.58 au, and a nine-month period when Voyager 2 traveled from 6.5 to 8.08 au. Then we combine these two time periods together to yield detection result for one full year. All the detection results are obtained by using the duration range from 9 to 2255 minutes under the scenario with thermal pressure included in the calculation except for Ulysses (Chen et al. 2019). Due to the 4-8 minute resolution of plasma data and 1 min magnetic field data, we switch off the thermal pressure for Ulysses in order to have a consistent comparison with other missions.

Table 2. Selection Criteria for Event Sets from Each Spacecraft Mission over One Full Year.

Spacecraft	Year	Radial Distance (au)	Walén Slope Threshold	$ \mathbf{B} $ (nT)	Counts
Helios 1 & 2	... ^a	0.3-0.4	0.3	≥ 25	2491
ACE	2004	~ 1.0	0.3	≥ 5	3049
Ulysses	2004	5.3-5.4	0.5	≥ 0.2	2620
Voyager 1 & 2	1980	6.5-8.1	0.5	-	1967

^aMultiple years from 1975 to 1981.

For the Helios and Voyager missions, the events are selected from both probes and some from multiple years in order to account for the significant number of data gaps while maintaining a narrow range of radial distances. The events from ACE and Ulysses are from the same and continuous one-year period in 2004 when they were radially aligned near the ecliptic plane (Chen et al. 2019). Figure 8 shows the distributions of duration and scale sizes for these selected events, respectively. Because of reduced event counts, the power-law distribution in each event set is not as pronounced as in each individual mission, e.g., as seen in Figure 1. They still exhibit power laws, especially in scale size distributions shown in Figure 8b, with different power-law slopes. The mean values seem to increase with radial distances, which ceases at about 7 au at Voyagers. The disruption of such an increase at Voyagers is likely due to the interruption in the continuous coverage of time-series data, which prohibits the detection of longer/larger event intervals, although these events are much fewer.

Figure 9 again shows collectively the corresponding SFR parameters. They generally exhibit variations largely owing to the varying radial distances. Their values span wide

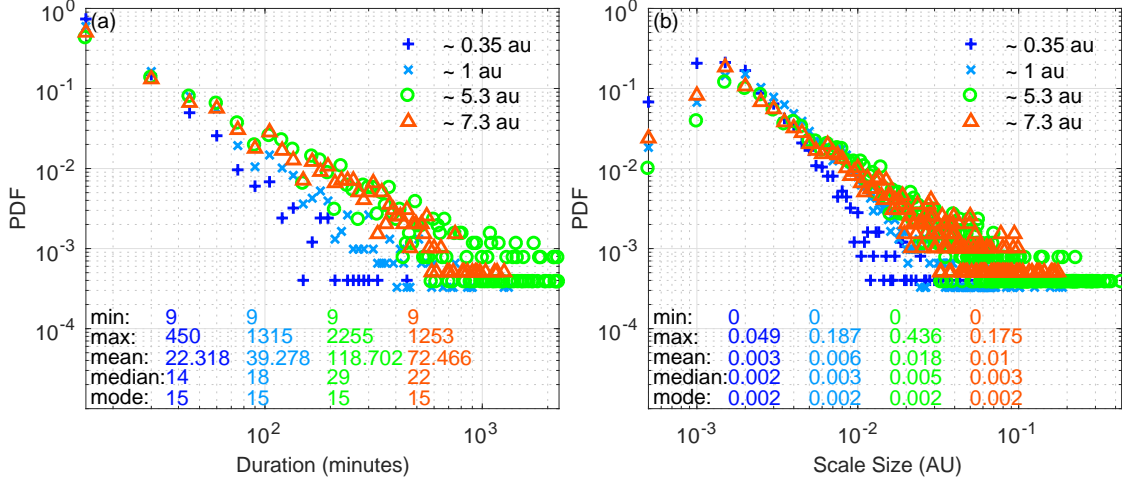


Figure 8. The distributions of (a) duration and (b) scale size for the **selected SFR** event sets listed in Table 2. Different symbols represent different missions at different radial distances as indicated by the legend. The statistical quantities for each distribution are denoted in each panel.

ranges, and are well separated for different radial distances. One exception is the proton $\langle\beta\rangle$, which exhibits much similar distributions among all the event sets, with the mean values of the same order of magnitude, $\gtrsim 0.1$, despite the wide separation in radial distances.

Finally, to examine and quantify the trend in radial variation for a few selected flux rope parameters, we show the radial variations of the average field magnitude $\langle B\rangle$, the average transverse field $\langle B_t\rangle$, and the axial field $\langle B_z\rangle$ over all flux rope intervals with associated uncertainties (standard deviations) for each event set at the corresponding radial distance r . A power-law fit in the form $\propto r^\alpha$ is also obtained for each quantity and the corresponding power-law indices are denoted, as given in Figure 10. They show a consistent trend of decaying with increasing radial distances, with the power-law indices $\alpha \approx -1.4$. This value falls between -1 and -2. The former number corresponds to the radially decaying power-law index for the azimuthal component of the nominal Parker spiral field, while the latter corresponds to that for the radial field.

4. RADIAL EVOLUTION OF MAGNETIC FLUX ROPES

One scenario for the radial evolution of SFRs is to consider flux rope merging associated with inverse magnetic energy transfer under the assumption that the poloidal magnetic flux A_m remains conserved. We choose a typical range of poloidal magnetic flux $A_m \in [0.5, 1.5]$ T·m and examine the corresponding radial evolution of selected properties. A preliminary analysis of the radial evolution of selected SFR properties (Chen et al. 2018) hinted at power-law decaying relations with respect to radial distance with power-law indices ranging from -1.5 to -0.5 for a wide range of A_m values. This quantity, A_m , represents the amount of poloidal magnetic flux per unit length (per meter) for a cylindrical flux rope, which is an output from our GS based search

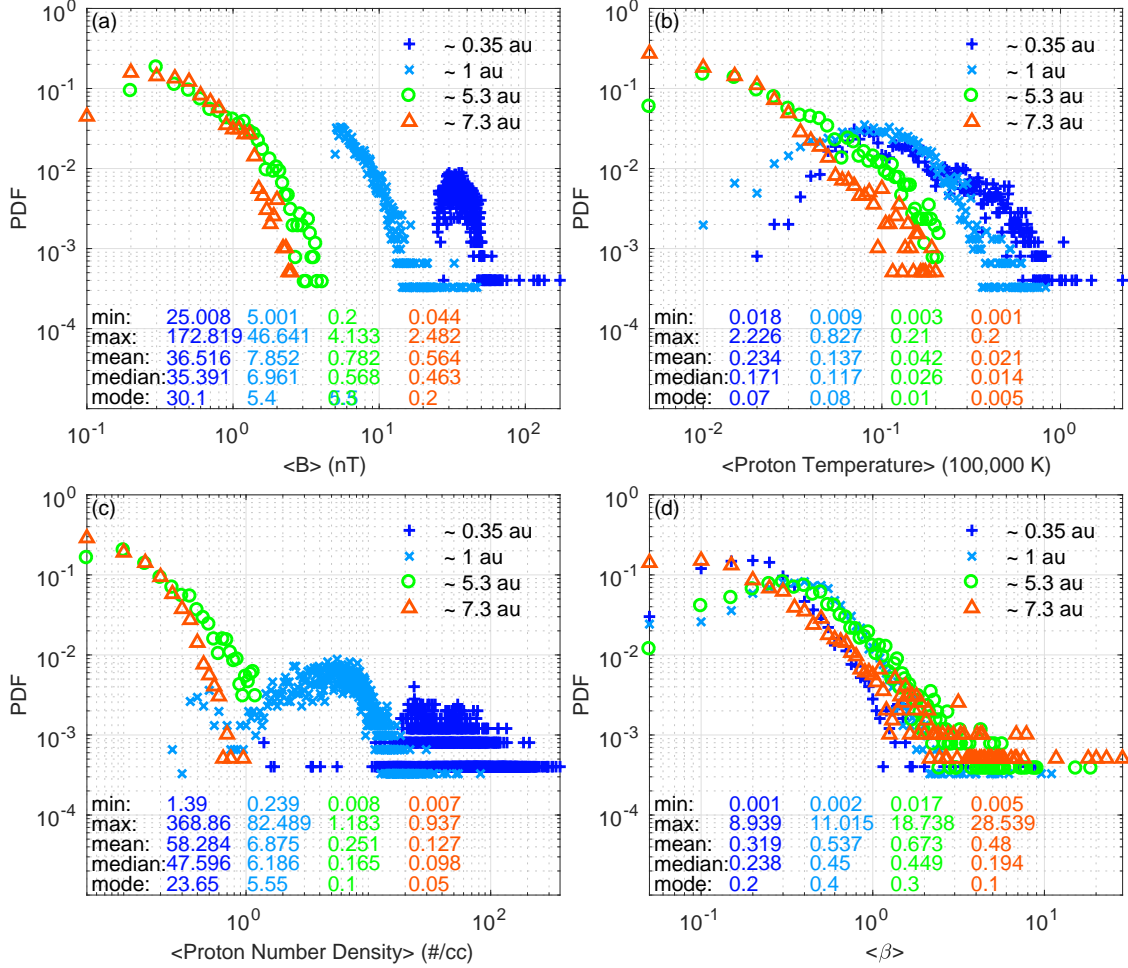


Figure 9. The distributions of SFR properties for the selected events listed in Table 2. Format is the same as Figure 3, except that the legend indicates the symbols for different missions at different radial distances.

algorithm and is directly derived from in-situ spacecraft measurements. It is simply the difference between two flux function values, one at the center and the other at the boundary of a flux rope.

In order to compare with the relevant theoretical work (e.g., Zhou et al. 2019), we consider a scenario of consecutive flux rope merging, leading to an increase in scale size but a decrease in magnetic field magnitude, while maintaining the poloidal magnetic flux. We further scrutinize our event sets by imposing the criterion for the unit poloidal magnetic flux, A_m , to be within $[0.5, 1.5]$ T·m, i.e., approximately a constant ~ 1 T·m with uncertainty. Such a value around 1 T·m is typical for an SFR in the solar wind. A quantitative case study of flux rope merging in interplanetary space was reported in Hu et al. (2019). It was found that given a dynamic evolution time on the order of 10^4 seconds for the two adjacent flux ropes to fully merge into one via magnetic reconnection, the reconnected magnetic flux during the process would be equal to the amount of the poloidal flux of each flux rope. If we take the typical value 1 T·m, then the reconnection rate can be estimated to be approximately $1/10^4$

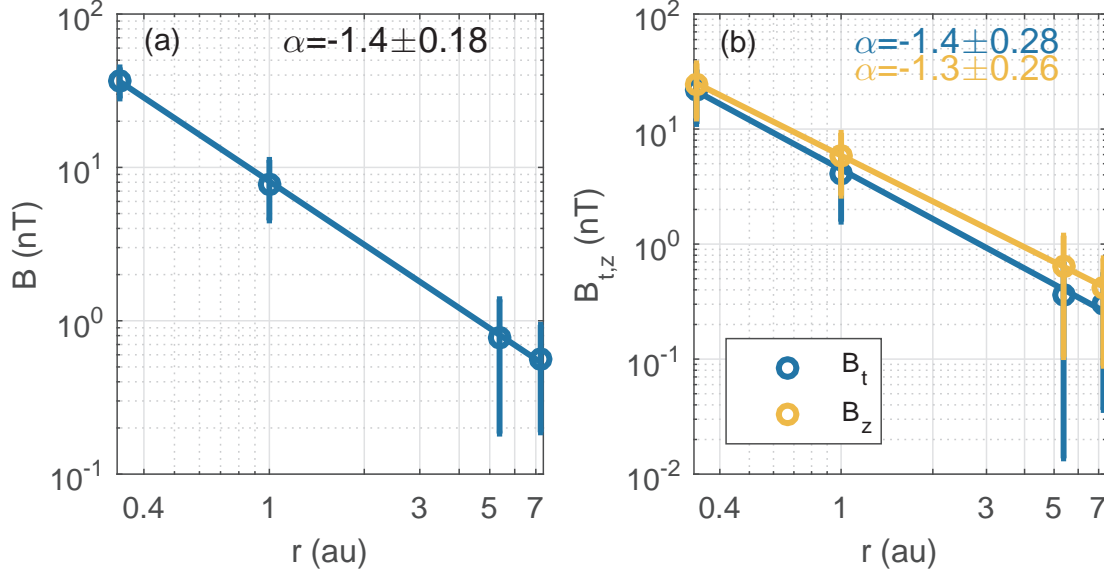


Figure 10. The radial dependence with the heliocentric distance r for (a) the average magnetic field magnitude, and (b) the corresponding transverse and axial component, respectively. The symbols with errorbars represent the averages over all selected flux rope intervals and associated standard deviations, while the solid lines represent the linear fits, $\propto r^\alpha$. The corresponding slopes (α) on the log-log scales are given.

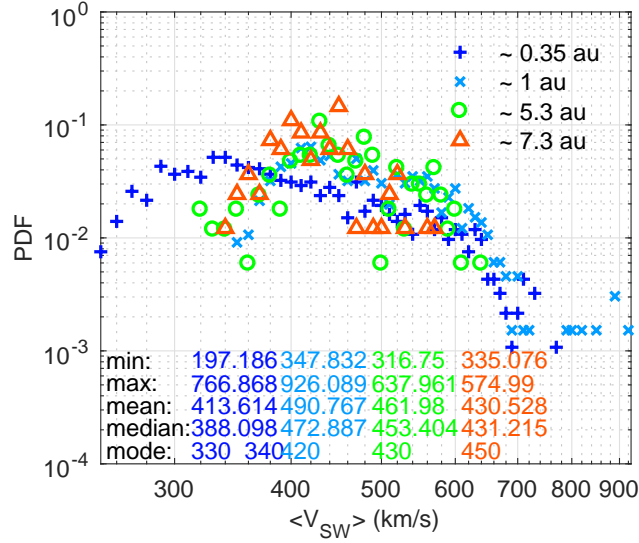


Figure 11. The distribution of the average solar wind speed, v_{sw} , for events listed in Table 3. Format is the same as Figure 7.

V/m or 0.1 mV/m, which is not unreasonable for the solar wind, given that a value on the order of $\lesssim 1$ mV/m was typically found for the reconnection events at the Earth's magnetopause (e.g., Hasegawa et al. 2010). Such a range also ensures a more certain flux rope configuration for the corresponding events by excluding the ones with small values of A_m (i.e., < 0.5 T·m), which are sometimes caused by a small rotating field component (B_y), indicating a less certain flux rope configuration. Additionally, for

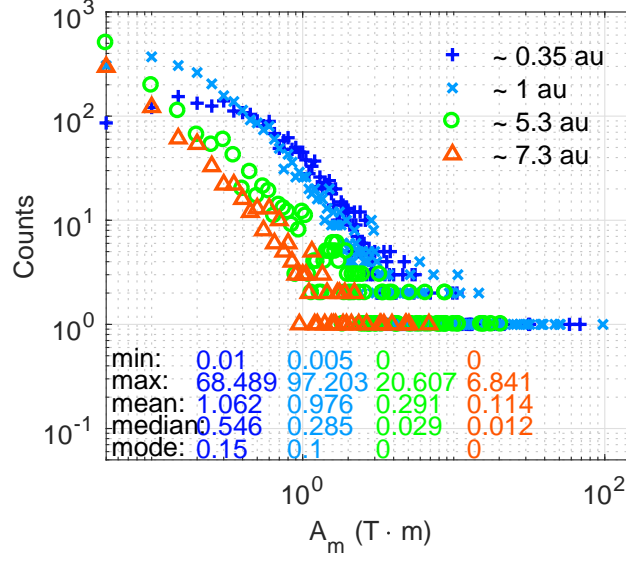


Figure 12. The distributions of the poloidal magnetic flux per unit length, A_m , for all the event sets listed in Table 2.

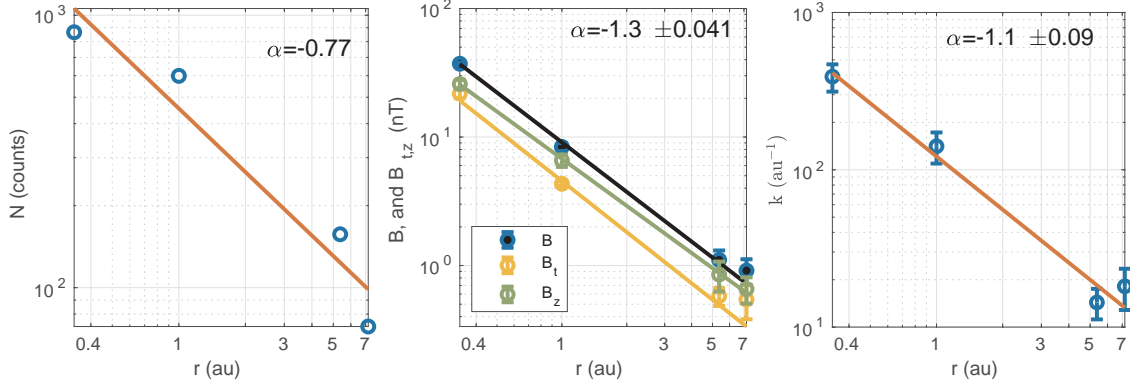


Figure 13. The radial dependence of the parameters listed in Table 3 (from the left to the right panels): the SFR event counts, the field magnitude, and the transverse and axial field components, respectively, and the inverse scale size. Format is the same as Figure 10.

the large-scale counterparts of SFRs, i.e., the MCs, the poloidal flux can amount to ~ 100 T·m, corresponding to total poloidal magnetic flux of the order of magnitude $\sim 10^{21-22}$ Mx that can be well related to the flux contents in solar source regions (Qiu et al. 2007; Hu et al. 2014).

Table 3. Radial distribution of the parameters with uncertainties for flux ropes with unit poloidal magnetic flux $A_m \in [0.5, 1.5]$ T·m.

r (au)	N	$\langle B \rangle \pm \Delta B$ (nT)	$k \pm \Delta k$ (au ⁻¹)	$\langle B_t \rangle \pm \Delta B_t$ (nT)	$\langle B_z \rangle \pm \Delta B_z$ (nT)
0.34	866	37±0.91	391±77	22±1.7	26±2.0
1.0	599	8.4±0.59	141±32	4.3±0.17	6.6±0.72
5.4	157	1.1±0.20	14±3.2	0.58±0.092	0.85±0.22
7.2	72	0.91±0.21	18±5.3	0.54±0.16	0.66±0.15

Figure 11 shows the corresponding solar wind speed distributions for these subsets of events. Again there are a significant number of events from Helios with relatively low speed around 300 km/s. Figure 12 shows the distributions of the poloidal magnetic flux A_m for the four spacecraft missions at different radial distances. They generally span a similar range with the maximum values in the order of tens of T·m, except for the Voyagers. The event counts generally decrease with increasing radial distances, especially for $A_m \gtrsim 0.5$ T·m. In Zhou et al. (2019), it was predicted that the time evolution of consecutive flux rope merging yields the following power laws in time, t ,

$$\bar{N} \sim t^{-1.0}, \quad \langle B \rangle \sim t^{-0.5}, \quad k \sim t^{-0.5}. \quad (1)$$

These quantities are the flux rope count \bar{N} over a 2D domain, the average magnetic field magnitude $\langle B \rangle$, and the inverse scale size k , under the condition that poloidal magnetic flux is conserved after merging. In other words, the amount of poloidal magnetic flux contained in each individual flux rope is not varying in time, although two neighboring flux ropes will merge into one consecutively. We intend to carry out an analysis from observations and the GS-based search result, following these conditions, with the additional assumption that the evolution in time as envisaged by Zhou et al. (2019) can be translated into the variation in radial distance, r , as we demonstrate below, by considering a constant radial solar wind flow. For instance, in Figure 11, the mean values among the average solar wind speed distributions for these events are similar. One obvious caveat that is also inevitable in this type of analysis of spacecraft data is the intrinsic radial change of the background field, i.e., the Parker interplanetary field in the solar wind, which was not incorporated in the theory of Zhou et al. (2019).

Table 3 summarizes the findings from the analysis of our unique event sets, with values of A_m strictly confined within the range $[0.5, 1.5]$ T·m. The list of parameters includes the event counts N , $\langle B \rangle$, k , $\langle B_t \rangle$, and $\langle B_z \rangle$ with associated uncertainties at the corresponding radial distances, r . These results are further illustrated in Figure 13 with the corresponding power-law fittings, $\propto r^\alpha$. The count N is obtained only along the radial dimension. In order to compare with the count predicted by Zhou et al. (2019) from their 2D simulations over a square area, we may compute N^2 to approximate such a count in 2D, i.e., $N^2 \approx \bar{N}$. This yields a power-law index $\alpha \approx -1.5$. Therefore, similar to what Zhou et al. (2019) obtained as given in equation (1), the radial evolutions of these quantities seem to obey the following power laws from our data analysis,

$$N^2 \sim r^{-1.5}, \quad \langle B \rangle \sim r^{-1.3}, \quad k \sim r^{-1.1}. \quad (2)$$

This set of power laws still differs significantly from those presented by Zhou et al. (2019), when assuming the equivalence between the radial distance r and time t .

5. SUMMARY AND DISCUSSION

In summary, we have carried out quantitative analysis of the interplanetary spacecraft mission data, in addition to the ACE/Wind and Ulysses missions, following the automated detection approach for the SFRs based on the GS reconstruction technique. The new results reported here yield the following total numbers of SFR event counts, respectively: 15,041 for Helios 1, and 7,981 for Helios 2 throughout their whole mission periods; 1,480 (1,991) for Voyager 1 (2) in year 1980 only. The SFR properties derived from each event set are summarized and presented via means of statistical analysis. Targeted studies using subsets of events are performed, especially for the purpose of examining the radial evolution of selected flux rope properties relevant to other works. Such a study is made feasible by including all derived event sets distributed over the range of heliocentric distances, namely, $r \in [0.3, 7]$ au, and the unique approach of characterizing SFRs by the amount of poloidal magnetic flux obtained through the GS reconstruction method. The main findings are summarized as follows.

1. The event occurrence rate is still on the order of a few hundreds per month, for the range of radial distances between 0.3 au and 7-8 au near the ecliptic plane.
2. The duration and scale size distributions of SFRs again exhibit power laws. They possess different power-law slopes at different radial distances.
3. The axis orientations of the identified cylindrical SFRs have broad distribution peaks grossly centered around the nominal Parker spiral field directions at different radial distances. The trend is more pronounced for the polar angles than for the azimuthal angles.
4. The bulk properties of SFRs, such as the average magnetic field magnitude, proton number density and temperature, generally exhibit clear decay in magnitudes with increasing radial distances, while the proton $\langle\beta\rangle$ remains largely unchanged.
5. The radial changes in magnetic field magnitudes, separately for the total field, the axial and the transverse components, seem to follow the general rule for a Parker magnetic field model, all with a power-law index close to -1.5.
6. For a uniquely controlled subset of SFR events with the corresponding unit poloidal magnetic flux $A_m \in [0.5, 1.5]$ T·m. The radial decaying in r for the following quantities, event counts N^2 , average field magnitude $\langle B \rangle$, and inverse scale size k , yields the corresponding power laws: $N^2 \sim r^{-1.5}$, $\langle B \rangle \sim r^{-1.3}$, and $k \sim r^{-1.1}$.

The radial change in magnetic field seems to be consistent with the theoretical and observational analysis of 2D MHD turbulence throughout the heliosphere. For instance, the theoretical work as well as the analysis of turbulence properties based on in-situ spacecraft observations by Zank et al. (2017); Adhikari et al. (2017);

Zhao et al. (2017) showed the radial change of fluctuating magnetic power, following largely a power law $\sim r^\gamma$ with the value $\gamma \approx 2\alpha$ lying between -2 and -3, consistent with $\alpha \approx -1.3$ to -1.4 for the magnetic field variations from our analysis results. In particular, the radial change of the correlation length scale in the ranges $r \in [0.3, 1]$ and > 1 au seems to follow mostly power laws with different power-law indices (Adhikari et al. 2017; Zhao et al. 2017). According to Zhao et al. (2017), the correlation length scale changes from about the order of $\lesssim 0.01$ au for $r \in [0.3, 1]$ au to about $\gtrsim 0.01$, approaching 0.1 AU for $r \in [1, 10]$ au, which is consistent with the change of the characteristic (average inverse) scale size of the SFRs from our analysis (see Figure 13) over these radial distances. It is also worth noting that the radial dependence of $k \sim r^{-1.1}$ should not be interpreted as indication of self-similar expansion, because this scale represents the dimension in the radial direction only, not the lateral (i.e., longitudinal or latitudinal) dimension, which has the r^{-1} dependence simply due to the radially outward flow. Therefore such a dependence for the radial dimension may hint at certain intrinsic processes at work subject to local conditions when examined separately at different radial distances. Generally speaking the apparent effect due to expansion in the radial dimension is under control by setting the Walén slope threshold in our approach, with which events with significant remaining flows, an indication of expansion, are excluded from our event sets.

Although there appears to be more events from Helios occurring in slow solar wind, there is also a trend of increasing Alfvénicity at closer radial distances to the sun, as indicated by the reduction in event counts (see Table 2) for Helios. A number of newly published studies have indicated the trend by using the PSP data but with different approaches (see, e.g., Kasper et al. 2019; Zhao et al. 2019). It is shown that the highly Alfvénic activity persisted in rather low-speed solar wind streams. How the nature of solar wind fluctuations changes with radial distance or different streams can be further elucidated by checking the newly acquired PSP data. The application of the GS-based automated SFR detection approach to the publicly available PSP data is currently ongoing.

ACKNOWLEDGMENTS

We are grateful to our colleagues at SPA/CSPAR, UAH, Drs. Laxman Adhikari, Jakobus le Roux, Gang Li, Gary Webb, Gary Zank, and Lingling Zhao for on-going collaborations. The Helios data are accessed via <http://helios-data.ssl.berkeley.edu/>. The other spacecraft data are provided by the NASA CDAWeb. We acknowledge NASA grants NNX17AB85G, 80NSSC19K0276, 80NSSC18K0622, and NSF grant AGS-1650854 for support. Special thanks also go to the SCOSTEP/VarSITI program for support of the development and maintenance of the on-line small-scale magnetic flux rope database website, <http://fluxrope.info>.

REFERENCES

- Adhikari, L., Zank, G. P., Hunana, P., et al. 2017, *The Astrophysical Journal*, 841, 85
- Borovsky, J. E. 2008, *Journal of Geophysical Research (Space Physics)*, 113, A08110
- Cartwright, M. L., & Moldwin, M. B. 2008, *Journal of Geophysical Research: Space Physics*, 113, doi:10.1029/2008JA013389, a09105
- Cartwright, M. L., & Moldwin, M. B. 2010, *Journal of Geophysical Research (Space Physics)*, 115, A08102, a08102
- Chen, Y., Hu, Q., le Roux, J., & Zheng, J. 2018, *Journal of Physics: Conference Series*, 1100, 012006
- Chen, Y., Hu, Q., & le Roux, J. A. 2019, *ApJ*, 881, 58
- Feng, H. Q., Wu, D. J., & Chao, J. K. 2007, *Journal of Geophysical Research: Space Physics*, 112, a02102
- Feng, H. Q., Wu, D. J., Lin, C. C., et al. 2008, *Journal of Geophysical Research: Space Physics*, 113, A12105, a12105
- Greco, A., Chuychai, P., Matthaeus, W. H., Servidio, S., & Dmitruk, P. 2008, *Geophysical Research Letters*, 35, doi:10.1029/2008GL035454, l19111
- Greco, A., Matthaeus, W. H., Perri, S., et al. 2018, *SSRv*, 214, 1
- Greco, A., Matthaeus, W. H., Servidio, S., Chuychai, P., & Dmitruk, P. 2009, *The Astrophysical Journal Letters*, 691, L111
- Hasegawa, H., Sonnerup, B. U. ., & Nakamura, T. K. M. 2010, *Journal of Geophysical Research: Space Physics*, 115, <https://agupubs.onlinelibrary.wiley.com/doi/pdf/10.1029/2010JA015679>
- Hau, L.-N., & Sonnerup, B. U. O. 1999, *Journal of Geophysical Research: Space Physics*, 104, 6899
- Hu, Q. 2017, *Sci. China Earth Sciences*, 60, 1466
- Hu, Q., Chen, Y., & le Roux, J. 2019, *Journal of Physics: Conference Series*, 1332, 012005
- Hu, Q., Qiu, J., Dasgupta, B., Khare, A., & Webb, G. M. 2014, *The Astrophysical Journal*, 793, 53
- Hu, Q., & Sonnerup, B. U. Ö. 2001, *Geophysical Research Letters*, 28, 467
- Hu, Q., & Sonnerup, B. U. O. 2002, *Journal of Geophysical Research: Space Physics*, 107, SSH 10
- Hu, Q., Zheng, J., Chen, Y., le Roux, J., & Zhao, L. 2018, *ApJS*, 239, 12
- Kasper, J. C., Bale, S. D., Belcher, J. W., et al. 2019, *Nature*, 576, 228
- Matthaeus, W. H., Bieber, J. W., Ruffolo, D., Chuychai, P., & Minnie, J. 2007, *ApJ*, 667, 956
- Moldwin, M. B., Ford, S., Lepping, R., Slavin, J., & Szabo, A. 2000, *Journal of Geophysical Research: Space Physics*, 105, 57
- Moldwin, M. B., Phillips, J. L., Gosling, J. T., et al. 1995, *Journal of Geophysical Research: Space Physics*, 100, 19903
- Osman, K. T., Matthaeus, W. H., Gosling, J. T., et al. 2014, *Physical Review Letters*, 112, 215002
- Pecora, F., Greco, A., Hu, Q., et al. 2019, *The Astrophysical Journal*, 881, L11
- Qiu, J., Hu, Q., Howard, T. A., & Yurchyshyn, V. B. 2007, *ApJ*, 659, 758
- Servidio, S., Matthaeus, W. H., & Dmitruk, P. 2008, *Physical Review Letters*, 100, 095005
- Sonnerup, B. U. O., & Guo, M. 1996, *Geophysical Research Letters*, 23, 3679
- Wan, M., Matthaeus, W. H., Servidio, S., & Oughton, S. 2013, *Physics of Plasmas*, 20, 042307
- Wang, W., Pappalardo, G., & Calvin, A. B., et al. 2016, *Journal of Geophysical Research: Space Physics*, 121, 5005
- Yu, W., Farrugia, C. J., Lugaz, N., et al. 2014, *Journal of Geophysical Research: Space Physics*, 119, 689
- Zank, G. P., Adhikari, L., Hunana, P., et al. 2017, *The Astrophysical Journal*, 835, 147

- Zhao, L.-L., Adhikari, L., Zank, G. P.,
Hu, Q., & Feng, X. S. 2017, *The
Astrophysical Journal*, 849, 88
- Zhao, L. L., Zank, G. P., Adhikari, L.,
et al. 2019, arXiv e-prints,
arXiv:1912.02349
- Zheng, J., & Hu, Q. 2018, *ApJL*, 852, L23
- Zhou, M., Bhat, P., Loureiro, N. F., &
Uzdensky, D. A. 2019, *Phys. Rev.
Research*, 1, 012004